Nanoscale β-nuclear magnetic resonance depth imaging of topological insulators

Dimitrios Koumoulis[a], Gerald D. Morris[b], Liang He[c], Xufeng Kou[c], Danny King[a], Dong Wang[d], Masrur D. Hossain[b,d], Kang L. Wang[c], Gregory A. Fiete[e], Mercouri G. Kanatzidis[f], and Louis-S. Bouchard[a,g,1]

[a]Department of Chemistry and Biochemistry, University of California, Los Angeles, CA 90095; [b]TRI University Meson Facility (TRIUMF), Vancouver, BC, Canada V6T 2A3; [c]Department of Electrical Engineering, University of California, Los Angeles, CA 90095; [d]Department of Physics & Astronomy, University of British Columbia, Vancouver, BC,Canada V6T 1Z1; [e]Department of Physics, University of Texas at Austin, Austin, TX 78712; [f]Department of Chemistry, Northwestern University, Evanston, IL 60208; and [g]California NanoSystems Institute, University of California, Los Angeles, CA 90095

Edited by Zachary Fisk, University of California, Irvine, CA, and approved June 5, 2015 (received for review February 4, 2015)

Considerable evidence suggests that variations in the properties of topological insulators (TIs) at the nanoscale and at interfaces can strongly affect the physics of topological materials. Therefore, a detailed understanding of surface states and interface coupling is crucial to the search for and applications of new topological phases of matter. Currently, no methods can provide depth profiling near surfaces or at interfaces of topologically inequivalent materials. Such a method could advance the study of interactions. Herein, we present a noninvasive depth-profiling technique based on β-detected NMR (β-NMR) spectroscopy of radioactive $^{8}Li^{+}$ ions that can provide "one-dimensional imaging" in films of fixed thickness and generates nanoscale views of the electronic wavefunctions and magnetic order at topological surfaces and interfaces. By mapping the ^{8}Li nuclear resonance near the surface and 10-nm deep into the bulk of pure and Cr-doped bismuth antimony telluride films, we provide signatures related to the TI properties and their topological nontrivial characteristics that affect the electron–nuclear hyperfine field, the metallic shift, and magnetic order. These nanoscale variations in β-NMR parameters reflect the unconventional properties of the topological materials under study, and understanding the role of heterogeneities is expected to lead to the discovery of novel phenomena involving quantum materials.

topological insulator | nuclear magnetic resonance | depth profiling | condensed matter physics | nanoscale physics

Topological insulators (TIs) are narrow-gap semiconductor materials that are insulating in the bulk and conductive on their surface. The constituent atoms are typically heavy elements with large spin–orbit coupling (SOC). In time-reversal–invariant materials, the electronic structure of TIs is characterized by band inversions from strong SOC at an odd number of time-reversal–invariant momenta in the bulk Brillouin zone. Unlike metals or ordinary insulators (OIs), charge carriers in TIs evolve from metallic to insulating as a function of depth from the surface. The surface-state electrons are characterized by a suppression of backscattering and an intrinsic chirality of spin-momentum locking, making them of interest in spintronics. A number of theoretical predictions of experimental observations have been made including Majorana fermions, condensed-matter axions, and quantized Hall conductance (1, 2). Heterostructure engineering, where a crystal is formed consisting of a sequence of different building blocks (for example, alternating TI and OI layers), can trigger new physical phenomena such as TIs with enhanced bulk band gaps (3) or Weyl semimetals (4).

Because topological materials are characterized by sharp changes in electronic properties at their surfaces and at interfaces with other materials, sensitive techniques are required to probe electronic and magnetic properties in a spatially resolved manner down to the atomic length scale. It has become clear that TI properties are spatially dependent (both in-plane and as a function of depth or film thickness). Magnetic phenomena are accompanied by inhomogeneities within the material and interactions at interfaces that cannot be explained by simple models. To date, the observation of metallic surface states has been accomplished with transport measurements, scanning tunneling microscopy (STM), and angle-resolved photoemission spectroscopy (ARPES) (5, 6). The depiction of the Dirac dispersion with ARPES requires *n*-type samples. Likewise, transport and STM require sufficiently conductive samples. Moreover, such experiments require the growth of high-quality samples (ideally, thin films or cleaved crystals exposing atomically flat surfaces) and often are most effective at low temperatures (<30 K) and for thin (<15 nm) layers. In addition, these techniques do not provide depth-resolved information. These factors limit their applicability in the study of complex heterostructures. Consequently, spatially resolved, noninvasive measurements of material properties would be an important asset in the study of physics at interfaces.

NMR has the potential to overcome some of the challenges associated with traditional characterization methods. Because it acts as a local probe of electron–nuclear hyperfine interaction with electrons near the Fermi level, it can depict the electronic and magnetic properties of insulating or metallic materials (*p*-type or *n*-type), does not require long-range crystal order, and does not rely on electron transport. NMR has been regarded as an unlikely candidate for the study of topological states because of the low dimensionality of thin films and associated sensitivity issues: the detection of solid-state NMR signals typically requires at least 10^{15} nuclear spins, whereas the nanometer-thick layers associated with topological surface states contain significantly

Significance

The surface states of topological insulators (TIs) and magnetically doped TIs exhibit considerable inhomogeneities at the nanoscale. Methods are needed to probe the degree of heterogeneity as a function of depth in nanoscale layers. We present a method that can directly visualize TIs in a depth-resolved manner and report on their electronic and magnetic properties. For example, in epitaxial thin films we demonstrate an increase in the density of states, a weakening of the ferromagnetic order when approaching the TI edges, as detected by measurements of the electron–nuclear hyperfine interaction, the effective *s–d* exchange integral, and local moment density. Depth profiling is expected to help uncover exotic physics of pure and ferromagnetic TIs and TI heterostructures.

Author contributions: D. Koumoulis and L.-S.B. designed research; D. Koumoulis, L.H., X.K., and L.-S.B. performed research; G.D.M., L.H., X.K., D.W., M.D.H., K.L.W., M.G.K., and L.-S.B. contributed new reagents/analytic tools; D. Koumoulis, G.D.M., L.H., X.K., D. King, G.A.F., and L.-S.B. analyzed data; and D. Koumoulis, G.D.M., X.K., G.A.F., M.G.K., and L.-S.B. wrote the paper.

The authors declare no conflict of interest.

This article is a PNAS Direct Submission.

[1]To whom correspondence should be addressed. Email: louis.bouchard@gmail.com.

This article contains supporting information online at www.pnas.org/lookup/suppl/doi:10.1073/pnas.1502330112/-/DCSupplemental.

fewer spins. A potential solution to the sensitivity problem is the technique of β-detected NMR (β-NMR) (*SI Results, β-NMR experiments*). β-NMR enables us to interrogate the wavefunction of the charge carriers while varying the energy of incident ions to control implantation depth. β-NMR is similar to muon-spin rotation spectroscopy, except that a $^8Li^+$ ion is used rather than a muon. The heavier mass of $^8Li^+$ enables better control of the ion position by controlling the energy of the incident ions. The implantation profile of the ions in high-Z materials is sharp and localized to layers that are tens of nanometers thick. The signal from such thin layers can be detected with β-NMR using highly polarized nuclear spins (>60%) and the high-efficiency detection of β-emissions. Furthermore, the longer half-life of the ^8Li isotope (838 ms) can reveal dynamics of magnetic field fluctuations or spin precessions over timescales longer than muons (half life, 2.2 μs) would allow. The only NMR studies of TI surface states published to date were done on nanocrystals (7) and nanowires (8), by inferring the TI properties in the limit of high surface-to-volume ratios. A recent study on Bi_2Se_3 performed at high magnetic fields provides the means of approaching the quantum limit in TIs via NMR (9). Because films grown by molecular beam epitaxy (MBE) and cleaved surfaces from single crystals are universally studied by most researchers, NMR experiments that directly interrogate TI properties in a depth-resolved manner beneath the surface of epitaxial TI films would be preferred, as they would enable comparison with the literature. Noninvasive NMR measurements of TI properties reflect intrinsic material properties and could even help in the study and control of spin-polarized electron states. Herein, we investigate the possibility of depth-resolved measurements of both electronic and magnetic properties of epitaxial TI films using the technique of β-NMR. This technique may enable sensitive, noninvasive studies of surfaces and interfaces in topological phases. Additional advantages of the β-NMR technique may include less stringent requirements in terms of carrier type and concentration, operating temperature (T), film thickness, and film quality, compared with existing tools.

Experimental Procedure

Epitaxial thin films of the TI bismuth antimony telluride (Bi,Sb)$_2$Te$_3$, and Cr-doped (~8%) (Bi,Sb)$_2$Te$_3$ (denoted CrTI below) with Bi/Sb ratios of 0.51/0.49 and 0.54/0.38, respectively, were grown on GaAs substrates (Fig. 1 *A* and *B*). The Bi-to-Sb ratio and the Cr doping level were deliberately chosen so that Fermi level positions of the as-grown samples are already close to the Dirac point (*SI Results,* section A). Accordingly, we were able to demonstrate and realize electrical conduction dominated by spin-polarized surface states (*SI Results,* section A), quantum interference competition (Fig. S1), quantum oscillation (*SI Results, Magneto-Transport Measurements*), quantum Hall effect (*SI Results, Magneto-Transport Measurements*), and quantum anomalous Hall effect (*SI Results, Magneto-Transport Measurements*) in the quantum limit regime. In this study, GaAs was chosen for two reasons. First, it is a suitable substrate for growth of this TI. Second, GaAs is a diamagnetic OI layer that provides an in situ reference for the β-NMR experiment, as probed by the beam energy of 19.9 keV. Its frequency shift as a function of depth and T via β-NMR experiments is well studied and understood (10). β-NMR measurements were conducted at the ISAC-I Facility (Isotope Separator and Accelerator) in TRI University Meson Facility (TRIUMF) (Vancouver, Canada) using a beam of highly polarized radioactive $^8Li^+$ ions. Beam energies in the range 0.4–19.9 keV were selected to probe the film properties as a function of depth (Fig. 1*A*). In the present study, the beam energy of 0.4 keV was used to probe primarily the surface layer of the TI film (~3–5-nm implantation depth), whereas the 1-keV beam probed the bulk of the TI (ions implanted ~10–20 nm deep). Higher beam energies were used to probe deeper layers into the OI substrate. For additional details of the experimental procedure, see *SI Results, β-NMR experiments*.

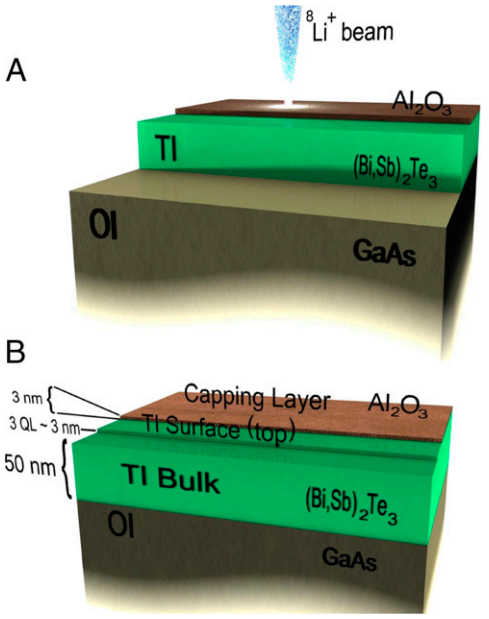

Fig. 1. Schematic diagram of the β-NMR experimental setup. The direction of the $^8Li^+$ ion beam and the different epitaxial layers are shown in *A*. Structure of the TI-OI multilayered (Bi,Sb)$_2$Te$_3$ sample [capping layer (<3nm Al_2O_3)], TI [50-nm (Bi,Sb)$_2$Te$_3$], and OI (350-μm GaAs) as a function of depth (nm) (*B*).

Results and Discussion

Electronic Properties. The Knight shift is an NMR parameter that probes the local polarization of conduction band electronic spins induced by an external field. The nuclear spins are coupled to the conduction band electrons through the hyperfine interaction, which is a measure of carrier density (11–13). Quantitative values of the Knight shift K_d are obtained by correcting the NMR resonance frequency shift, $K = (\nu - \nu_{ref})/\nu_{ref}$, for the demagnetization field, $(8\pi/3)\cdot\chi$, in the thin film (Fig. S2) according to

$$K_d = K + \left(\frac{8\pi}{3}\right)\cdot\chi, \qquad [1]$$

where χ is the magnetic susceptibility. K arises from coupling the $^8Li^+$ to the temperature (T)-independent Pauli susceptibility of the host nuclei, relative to the GaAs in situ reference. Similar to GaAs, (Bi,Sb)$_2$Te$_3$ is diamagnetic and exhibits a weak T-dependent magnetic susceptibility. Using the value of χ for (Bi,Sb)$_2$Te$_3$ reported by Stepanov et al. (14) and Van Itterbeek et al. (15), we note that in the data from refs. 14 and 15 χ follows a diamagnetic behavior over the range 2–300 K. The values of the Knight shift are plotted in Fig. 2*A* (*Upper Inset*) relative to the GaAs reference (*SI Results, β-NMR experiments*). An alternate graphical presentation of these results for the pure TI is also shown in Fig. S3. The salient feature of this result is the substantially larger (negative) Knight shift near the surface of the TI film compared with the bulk (Figs. S4 and S5). Such increased metallic shifts when approaching the surface of a TI are consistent with results from a previous study of diamagnetic Bi_2Te_3 nanocrystals (7). Knight shift measurements on $Bi_{0.5}Sb_{1.5}Te_3$ nanocrystals with conventional NMR (Fig. S6*A*) also confirm the emergence of a negative Knight shift (*SI Results, β-NMR experiments*) at the exposed surface. In the case of a metal, the wavefunction of delocalized charge carriers interacts with the nuclear spins through the electron–nuclear hyperfine interaction. Therefore, nuclear spins experience the average field of the electronic spin polarization, which leads to the Knight shift.

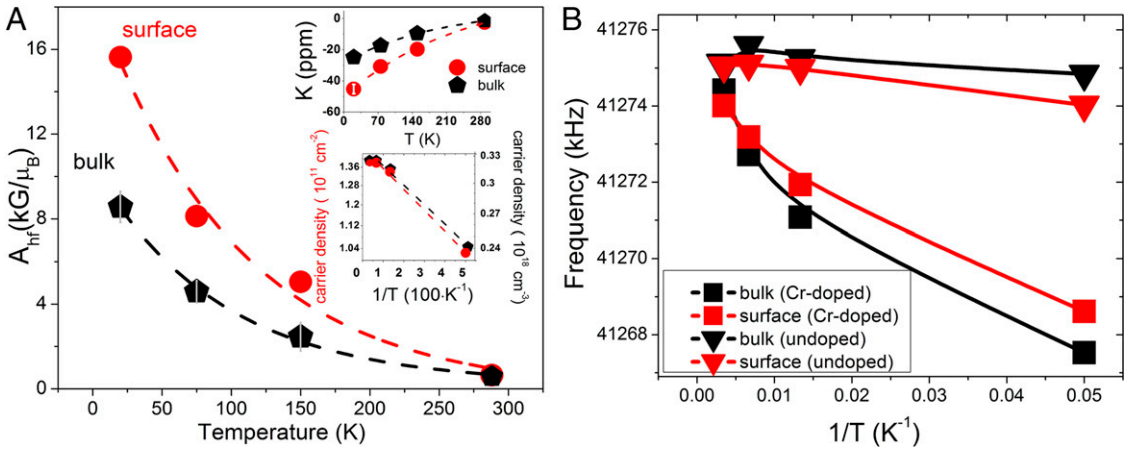

Fig. 2. Depth and temperature (*T*) dependence of the hyperfine coupling constant (A_{hf}). Surface and bulk measurements were made at beam energies of the surface (0.4 keV) and bulk (1 keV), respectively. (*Upper Inset*) The Knight shift (*K*) as a function of *T* for surface (red circles) and for 1 keV (black polygons) with respect to the resonance position of GaAs (19.9 keV, an in situ reference) (*A*). (*Lower Inset*) Estimates of the local carrier density. β-NMR response of the CrTI film compared with undoped TI as a function of depth and inverse temperature (*B*). Error bars are smaller than the symbol sizes for all figures.

The expression for the Knight shift in a degenerate semiconductor is (16–18)

$$K = \frac{4\pi}{3} g \cdot g^* \cdot \mu_B^2 \cdot \left\langle |u_k(0)|^2 \right\rangle_{E_0} \rho(E_F), \qquad [2]$$

where g, g^* are electron g factors (*vide infra*), $\rho(E_F)$ is the density of states at the Fermi level, and $\langle |u_k(0)|^2 \rangle_{E_0}$ is the single-particle free-electron probability density at the nucleus. The latter is averaged near the bottom of the conduction band for electrons or near the top of the valence band for holes (17) and depends on the origin of the hyperfine interaction (Fermi contact, dipolar, or orbital) (16). In our case, the nuclei are high-Z elements, and the relativistic effects on the hyperfine coupling are of major importance (16). Therefore, the term $\langle |u_k(0)|^2 \rangle_{E_0}$ should be relativistically expressed as $(\cos^2\theta^+)\langle R|\Delta(\vec{r})|R\rangle$, where $\cos\theta^+$ is a spin–orbit mixing parameter, R is the spatial atomic wavefunctions near the nucleus, and $\Delta(\vec{r})$ replaces the Dirac function $\delta(\vec{r})$. The typical Knight shift is proportional to the paramagnetic susceptibility, although this proportionality is valid only for a scalar g matrix (16). The spin–orbit parameter mixes the electronic wavefunctions, thus mixing the hyperfine contributions that generate the Knight shift. In the nonrelativistic approximation the hyperfine Hamiltonians use the free-electron g factor rather than the modified g^* because of the spin–orbit interaction and the crystalline potential (16). The magnitude and sign of the Knight shift in a narrow-gap semiconductor are governed by the carrier density and the (large) g^* factors of the carrier types, respectively. Eq. **2** underestimates the Knight shift because it neglects demagnetization field effects near the TI surface and the nonparabolicity of the multivalley band structure, which modulates the dependence between the Knight shift and the carrier density (16–18).

The electron–nuclear hyperfine coupling constant A_{hf} and the Knight shift K are related by

$$A_{hf} = \frac{K \cdot N_A \cdot \mu_e}{n \cdot \chi}, \qquad [3]$$

where N_A is Avogadro's number, n is the average coordination number at the implantation site, and μ_e is the magnetic moment of the charge carriers (19). We use the value $n = 2.4$ reported for lattice sites in Bi_2Te_3 (20). The hyperfine coupling, which is a local probe of the electronic wavefunctions in the vicinity of implanted $^8Li^+$ ions, is mediated by the strong SOC between the nuclei and the p-band carriers (11, 16, 21, 22). The hyperfine constants are plotted in Fig. 2*A*. We observe a T-dependent A_{hf}, which approximately doubles from the TI bulk (1 keV) to the TI surface (0.4 keV) that holds over the entire temperature range. This doubling indicates a higher (2×) carrier concentration at the TI surface compared with the TI bulk. We note that the hyperfine coupling constant of $^8Li^+$ measured near the surface of the TI approaches the value measured in a thin metallic silver film (19), 20.5 kG/μ_B (octahedral site) at low T. These results are consistent with transient reflectivity studies of Bi_2Se_3 thin films with varying thicknesses. These previous studies revealed a similar insulator (bulk TI) to metal (surface TI) cross-over with the film thickness decreasing from 25 to 6 nm. In addition, the ultrafast carrier dynamics at the surface (~6 nm) reached values comparable to those observed in noble metals (23).

Similarly, the behavior of a trivial insulator under β-NMR is qualitatively different from that of the TI. In contrast with the observed increased metallic shift when approaching the surface of a TI, β-NMR studies of MgO (a trivial insulator) thin films yielded no evidence of depth dependence of its resonance frequency as a function of beam energy (Fig. S5). Other detailed NMR studies of the Knight shift and relaxation in PbTe (E_g = 0.32 eV, 300 K) and Tl_2Se (E_g = 0.6 eV, 300 K) were consistent with a decrease in carrier concentration in nanoscale materials compared with bulk materials (24, 25), in contrast with the behavior observed in TI nanocrystals. Furthermore, in the case of ZnTe (E_g = 2.23 eV, 300 K) the ^{125}Te frequency shift of *nano*-ZnTe remains unshifted relative to micrometer-sized samples (Fig. S6*C*). Finally, in a β-NMR investigation in GaAs (E_g = 1.4 eV, 300 K) in which the effect of implantation energy was studied, no detectable Knight shift was reported in the case of *n*-GaAs, as the beam energy decreased from 28 to 3 keV (26). In that same study, no concomitant line broadening was observed, as would be expected of a transition to a metallic state. The lack of line broadening is in clear contrast with the TI layer depth-resolved properties measured in this study. This collection of experiments on trivial insulator surfaces and nanocrystals (see also Figs. S7–S9) clearly indicates distinctly different and nonmetallic behavior compared with the phenomena observed at the surface of the TI.

The estimates of the Knight shift by Eq. **2** (Fig. 2, *Inset*) are reasonably close to values previously reported (27, 28) in transport studies, namely, ~10^{19} cm^{-3} for Bi_2Te_3 and ~10^{18} cm^{-3} for $(Bi,Sb)_2Te_3$ thin films. Surface carrier concentrations were reported to be in the range 10^{11}–10^{12} cm^{-2} (27–29), of the same

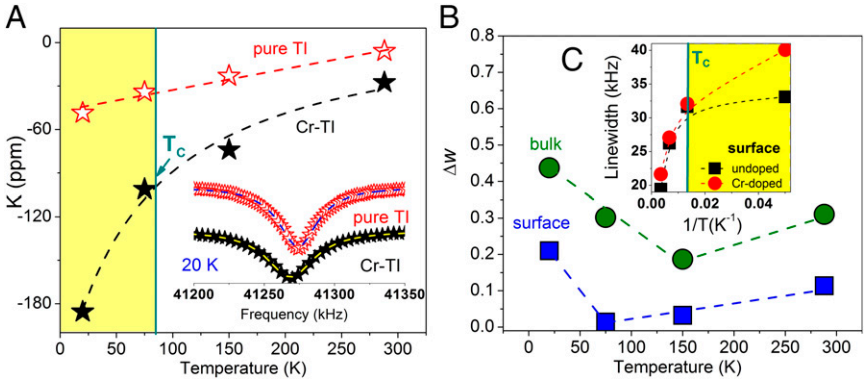

Fig. 3. Temperature dependence of Knight shift and relative linewidth at the surface of TI and CrTI. (*A*) Temperature dependence of Knight shift at the surface of pure TI (open red stars) and Cr-doped TI (filled black stars) measured with β-NMR. (*Inset*) β-NMR spectra at 20 K. (*B*) Temperature dependence of the relative linewidth parameter of $^8Li^+$ for beam energies 0.4 keV (blue squares) and 1 keV (green circles). (*C*) The temperature dependence of the linewidth for surface of undoped (black squares) and Cr-doped TI (red circles) reflects the effect of Cr dopants below 75 K. Experimental uncertainties are smaller than the symbols for all displayed figures.

order as observed here. Higher carrier concentrations at higher temperatures (150–288 K) have been commonly observed in narrow-gap semiconductors and are attributed to a cross-over from a thermally activated regime to a saturation regime.

A plot of the linewidth as a function of T and beam energy is shown in Figs. S2 and S3*B*. In the GaAs layer, the dependence of the linewidth on temperature is considerably small, similar to results from previous β-NMR studies in intrinsic GaAs (10). However, in the TI layer (0.4–1 keV), the linewidth is more than three times greater than in GaAs. We also note that the linewidth in the TI layer increases with decreasing T, in contrast with the non-TI material, GaAs (10). Another feature we observe is a considerably broader linewidth for the TI surface layer compared with the TI bulk, a result that is opposite of that observed for trivial (non-TI) semiconductors (26).

Magnetic Properties. We now turn our attention to the magnetic properties and examine the case of the Cr-doped TI thin film. The ability of β-NMR to differentiate pure TI from magnetic TI is clearly demonstrated by the T dependence of the Knight shift (Fig. 3*A*) and linewidth (Fig. 3*C*), which is substantially different for these two films, from 20 K up to ambient T. This trend is compatible with the development of magnetic correlations, which grow progressively stronger as T is lowered.

The second observation is that in the undoped TI, signals near the surface exhibit a larger negative Knight shift than in the TI bulk, whereas with Cr doping the opposite is true; no increase in Knight shift is apparent at the surface (Figs. S2 and S4*A*), consistent with the behavior of gapped surface states. In the Cr-doped TI, the Knight shift is promoted by the 3*d* spins (transferred field), diamagnetic core contributions, as well as *s*-like contributions from conduction electrons. The ^8Li β-NMR frequency as a function of temperature describes the influence of the Cr dopants. We observe an inflection point near 75 K for the surface layer and 150 K for the bulk-like layer that is due to the loss of magnetic order. Previous studies via magnetic and transport characterizations have predicted a robust ferromagnetism close to room temperature for Cr–Bi_2Te_3, ∼100 K for Bi_2Se_3:Mn, and up to 190 K for $Sb_{2-x}Cr_xTe_3$ (30–34). In nonzero external magnetic fields, the loss of magnetic order tends to be more extensive and shifts to higher temperatures compared with the case of a zero external field (31–36) owing to the creation of large local fields both above and below the critical temperature. Although no proper phase transition occurs in nonzero external fields in terms of critical phenomena (37), demagnetization nonetheless occurs, and we write "T_c" to refer to the region of inflection.

We now discuss the line broadening. In the β-NMR experiment, the presence of magnetic moments at the dopant sites will generate local internal fields that broaden the ^8Li β-NMR resonance. This broadening is proportional to the magnitude of the local magnetic moment density and reflects the distribution of this field. Whereas the frequency shift reflects the average field within the measurement region, the linewidth reflects the rms field fluctuation. To exclude nonmagnetic sources of line broadening such as a quadrupolar broadening (because $^8Li^+$ has a small quadrupole moment), power broadening, etc., we perform the analysis of the fractional broadening as defined by the relative linewidth parameter $[\Delta w = (W_{CrTI} - W_{TI})/W_{TI}]$, where W_{TI} is the linewidth of the ^8Li resonance in the TI film and W_{CrTI} is its linewidth in the Cr-doped TI film.

The results for Δw are shown in Fig. 3*B*. For the surface layer, the temperature dependence of linewidth, in accordance with the resonance shift, unveils the onset of a disparity near 75 K (Fig. 3*B*). Notably, the ^8Li β-NMR line broadens in the surface and bulk regions by approaching the transition temperature from below. This important observation may be associated with the presence of a small amount of local ordering that causes appreciable dipolar broadening above T_c. However, the possible presence of lattice distortions and strain effects in thin films cannot be completely excluded. At 1-keV energies (in the CrTI bulk), Δw suggests that the magnetic transition T_c occurs near 150 K, approximately two times higher. This result is consistent with the prediction of molecular-field theory that T_c should be proportional to the number of nearest neighbors, which is two times larger in the bulk than on the surface (35). Zhang and Willis (38), Voigt et al. (39, 40), and Rausch and Nolting (41), using differential perturbed angular correlation measurements of the magnetic hyperfine field in the topmost Ni monolayer and that in the deeper layers, also reported a similar increase in T_c. Similarly, we observed the transition temperature to decrease with decreasing penetration depth. This decrease in temperature could be due to the reduced disorder-causing fluctuations and smaller coordination number at the surface relative to the bulk.

The T dependence of Δw yields an estimate of the magnitude of the effective *s*–*d* exchange integral (J) by the relation $(W_{CrTI} - W_{TI})/W_{TI} = (Jp^2C/3gk_B) \cdot (1/T) + D$, where p is the effective number of Bohr magnetons, C is the atomic fraction of paramagnetic atoms, D is a temperature-independent term, k_B is the Boltzmann constant, and g is the g factor (39, 40). This relationship

provides the value of J that emerges from the Cr localized moments in the $(Bi,Sb)_2Te_3$ matrix. The slopes $(Jp^2C/3gk_B)$ were found to vary slightly from $(Jp^2C/3gk_B)^{bulk} = 5.07 \pm 1.76$ K for the bulk to $(Jp^2C/3gk_B)^{surface} = 4.53 \pm 1.05$ K for the surface layer; specifically, we observed that $J^{surface} = 0.9 \cdot J^{bulk}$. The value of the J ratios (0.9) suggests that not only the chromium density but also the carrier density should be considered when describing the line broadening on the surface and in the bulk layer. The Rudermann–Kittel–Kasuya effect is approximately the same order of magnitude as the nuclear dipolar interaction. Therefore, the present results do not rule out the possibility of a contribution from carrier-mediated ferromagnetism because both the hole/electron concentration and the chromium density drastically affect the T_c values independently (30–33). The presence of Cr in chalcogenides likely functions as a donor and increases the charge carrier concentration; therefore, our results are consistent with carrier-mediated magnetism in the surface of the Cr-doped TI film. In the case of different dopants, trends for T_c as a function of film thickness were reported by using different techniques. For comparison, we mention the results of Zhang and Willis based on measurements of bulk film magnetism through the magneto-optical Kerr effect (38), which were theoretically verified by Rausch and Nolting (41) in the molecular field approximation (Weiss mean-field theory) of the Heisenberg model. Furthermore, a recent ferromagnetic resonance study of Bi_2Se_3:Mn has revealed a stronger ferromagnetic order in the bulk than on the surface, which was attributed to the bulk layer being more homogeneously doped than the surface layer (34), in agreement with our observation. This result is also consistent with the larger fractional broadening Δw for the 1-keV beam (bulk of the TI) compared with the 0.4-keV beam (near TI surface), recalling that the fractional broadening is indicative of local moment density.

Compared with other techniques, our experimental procedure differs mainly in that rather than varying the film thickness, the reading is performed noninvasively, that is, as a function of depth, and in a film of fixed thickness. This experimental aspect is missing, for example, in ARPES and STM. Therefore, the β-NMR spectroscopy is an efficient and valuable tool for TIs whose topological properties depend strongly on film thickness or for TI layers that are part of a nanoscale device or heterostructure.

Conclusions

This depth-dependent study of electronic and magnetic properties of TI epitaxial layers using implanted $^8Li^+$ ions reveals important details about nanoscale layers. Namely, transitioning from bulk to the surface of the TI across a distance shorter than 10 nm, the electron–nuclear hyperfine coupling constant A_{hf} approximately doubles, reaching a value ∼16 kG/μ_B at 20 K, which is comparable to certain pure metals, intermetallic and cuprate compounds. This A_{hf} doubling is accompanied by a large negative Knight shift and line broadening, both of which phenomena approximately double from bulk to surface. The advantage of the β-NMR output was most effectively illustrated by noninvasively extracting the magnetic properties of the TI as a function of depth. As a function of temperature, the linewidth of the TI departs from that of the CrTI at ∼75 K (for the surface region) and 150 K (for the bulk region) because of the presence of Cr dopants, a result consistent with a gapped TI surface. The CrTI exhibited a 10% decrease in the effective s–d exchange integral when moving from the bulk to the surface, a decrease that is explained by carrier-mediated magnetism. This experimental approach could prove useful to understanding depth-dependent interactions, proximity-induced phenomena across interfaces and heterostructures in TIs, crystalline insulators, topological superconductors, and interaction-driven topological phases.

Materials and Methods

Thin-Film Heterostructures Growth. $(Bi,Sb)_2Te_3$ thin films were conducted in a Perkin-Elmer MBE system under ultrahigh vacuum conditions. Intrinsic GaAs (111)B wafers ($\rho > 10^6$ Ω·cm) were cleaned by a standard Radio Corporation of America procedure before being transferred into the growth chamber. GaAs substrates were annealed in the chamber under Se-protective environment at ∼580 °C for 30 min. During growth, Bi, Sb, and Te cells were kept at 470, 395, and 320 °C, respectively, while the GaAs (111) substrate was kept at 200 °C (growth temperature). After growth, 1.5 nm of Al was subsequently deposited in situ at 20 °C to protect the epilayer from unintentional doping in the ambient environment. Al film was later naturally oxidized to form Al_2O_3 after the sample was taken out of the chamber and exposed to air. After oxidation, the final thickness of the Al_2O_3 capping layer was ∼3 nm. The samples were cut to size 8 mm × 8 mm × 0.35 mm and mounted on sapphire substrates to provide good thermal contact and enable alignment of the $^8Li^+$ beam.

Magneto-Transport Measurements. Four-point Hall measurements were conducted using a Quantum Design physical property measurement system (PPMS) at the base temperature of 1.9 K. This setup enables us to systematically adjust several experimental variables such as temperature, magnetic field, measurement frequency, external gate bias, etc. Multiple lock-in-amplifiers and Keithley source meters were connected to the PPMS system, enabling compressive and high-sensitivity transport measurements. The samples used for transport measurements were patterned as thin-film Hall bar devices.

ARPES. The electronic structure of the $(Bi,Sb)_2Te_3$ thin film was studied by ARPES. The measurements were performed at BL12.0.1 of the Advanced Light Source Division (Lawrence Berkeley Laboratory, Berkeley, CA). Samples (without Al capping) for ARPES were further conditioned by mild annealing at T = 200 °C in the experimental chamber for 2 h. All photoemission data were collected from the samples at 10 K.

β-NMR. The β-NMR experiment was performed at the ISAC-I Facility radioactive ion beam facility (TRIUMF, Vancouver, Canada) using a beam of highly spin-polarized radioactive $^8Li^+$ ions (lifetime τ = 1.2 s, I = 2, gyromagnetic ratio $\gamma/2\pi$ = 6.3015∼MHz/T). The high magnetic field spectrometer (up to 9 T) is mounted on a high-voltage platform allowing the application of a retarding electrostatic potential, slowing the incoming $^8Li^+$ ions before implantation into the sample. Beam energy can be adjusted from 20 keV down to 0.33 keV for depth-resolved investigations. Samples were mounted on a coldfinger cryostat situated at the center of the magnet and in vacuum of 10^{-10} mbar. Nuclear polarization—initially antiparallel to beam momentum—was monitored via the parity-violating β-decay of the ^8Li nucleus ($^8Li \rightarrow {}^8Be + e^- + \overline{\nu_e}$) in which the momenta of outgoing betas are correlated with the instantaneous orientation of nuclear spin. Two beta-particle detectors situated upstream (B) and downstream (F) with respect to the sample recorded the decay events. The experimental signal proportional to nuclear polarization is the asymmetry in decay events counted by the two beta detectors, $P \propto (n_B - n_F)/(n_B + n_F)$. β-NMR spectroscopy was carried out at a fixed magnetic field (H_0 = 6.55∼T, applied normal to the sample face) by slowly stepping the radiofrequency (rf) magnetic field (H_1 = 35 μT parallel to the sample face) repeatedly up and down through the resonance condition at a rate of 2 kHz/s. Each run accumulated ∼5 × 10^9 events. Near resonance, incoherent transitions among the nuclear spin states driven by the continuous rf result in the destruction of nuclear polarization and a dip in asymmetry. The β-NMR lineshape reflects the magnetic field distribution probed by the ^8Li within the thin film.

ACKNOWLEDGMENTS. L.-S.B. acknowledges useful discussions with S. D. Mahanti. D. Koumoulis acknowledges W. A. MacFarlane and R. Kiefl for their help and guidance during the β-NMR experiments and for providing the MgO results ahead of publication, as well as B. Leung and R. E. Taylor for their help during the NMR and powder X-ray diffraction studies on Bi_2Te_3 and Sb_2Te_3. D. Koumoulis acknowledges B. J. Archer for drawing the illustration of Fig. 1. The research at University of California, Los Angeles (UCLA) and Northwestern University was funded by Defense Advanced Research Planning Agency (DARPA) MESO (MESOdynamic Architectures), Award 66001-12-1-4034. The magnetometry measurements were funded by Air Force Office of Scientific Research and DARPA QuASAR (Quantum-Assisted Sensing and Readout). G.A.F. was funded under Army Research Office W911NF-14-1-0579 and NSF DMR-0955778. All authors acknowledge the use of instruments at the Molecular Instrumentation Center facility at UCLA.

1. Moore JE, Balents L (2007) Topological invariants of time-reversal-invariant band structures. *Phys Rev B* 75(12):121306.
2. Hasan MZ, Kane CL (2010) Topological insulators. *Rev Mod Phys* 82(4):3045–3067.
3. Nakayama K, et al. (2012) Manipulation of topological states and the bulk band gap using natural heterostructures of a topological insulator. *Phys Rev Lett* 109(23):236804.
4. Burkov AA, Balents L (2011) Weyl semimetal in a topological insulator multilayer. *Phys Rev Lett* 107(12):127205.
5. Kong D, et al. (2011) Ambipolar field effect in the ternary topological insulator $(Bi_xSb_{1-x})_2Te_3$ by composition tuning. *Nat Nanotechnol* 6(11):705–709.
6. Zhang J, et al. (2011) Band structure engineering in $(Bi_{1-x}Sb_x)_2Te_3$ ternary topological insulators. *Nat Commun* 2:574.
7. Koumoulis D, et al. (2013) NMR probe of metallic states in nanoscale topological insulators. *Phys Rev Lett* 110(2):026602.
8. Nisson DM, Dioguardi AP, Peng X, Yu D, Curro NJ (2014) Anomalous nuclear magnetic resonance spectra in Bi_2Se_3 nanowires. *Phys Rev B* 90:125121.
9. Mukhopadhyay S, et al. (2015) Hyperfine coupling and spin polarization in the bulk of the topological insulator Bi_2Se_3. *Phys Rev B* 91(8):081105.
10. Dunlop T, et al. (2007) ^{8}Li in GaAs studied with β-NMR. *Physica B* 401:254–257.
11. Watson RE, et al. (1971) Comments on the Knight shift in bismuth and other *p*-band diamagnetic metals. *Phys Rev B* 3(1):222–225.
12. Das TP, Sondheimer EH (1960) Diamagnetic shielding of nuclei in metals. *Philos Mag* 5(53):529–531.
13. Barth S, et al. (1989) Diamagnetism and muon Knight shift in semimetallic and semiconducting BiSb single crystals. *Hyperfine Interact* 51(1-4):881–890.
14. Stepanov NP, Nalivkin VU, Potapov GA (2012) Magnetic susceptibility of $(Bi_{2-x}Sb_x)Te_3$ ($0<x<1$) alloys in the temperature range 2 to 50 K. *Semiconductors* 46(1):22–28.
15. Van Itterbeek A, Van Deynse N, Herinckx C (1966) Measurements on the magnetic anisotropy of single crystals Bi_2Te_3, Sb_2Te_3 and compounds of them, between room temperature and 1.3 K. *Physica* 32(11-12):2123–2128.
16. Leloup J, Sapoval B (1973) Knight shift in multivalley semiconductors. I. Theory of contact, orbital, and dipolar shift and relativistic effects. *Phys Rev B* 7(12):5272–5276.
17. Vieth HM, Vega S, Yellin N, Zamir D (1991) Temperature dependence of the NMR line shifts and T1 relaxation times of ^{125}Te in the semiconductor alloys $Hg_{1-x}Cd_xTe$. *J Phys Chem* 95(3):1420–1424.
18. Shi J, Wessels M, Ross JH, Jr (1993) Band-edge properties of a semiconductor alloy: An NMR study of $Hg_{1-x}Cd_xTe$. *Phys Rev B Condens Matter* 48(12):8742–8746.
19. Morris GD, et al. (2004) Depth-controlled β-NMR of ^{8}Li in a thin silver film. *Phys Rev Lett* 93(15):157601.
20. Sathyamoorthy R, Dheepa J (2007) Structural characterization of thermally evaporated Bi_2Te_3 thin films. *J Phys Chem Solids* 68(1):111–117.
21. Gygax FN, et al. (1984) Positive muons in antimony bismuth alloys. *Hyperfine Interact* 17(1-4):387–392.
22. Yavorsky BY, Hinsche NF, Mertig I, Zahn P (2011) Electronic structure and transport anisotropy of Bi_2Te_3 and Sb_2Te_3. *Phys Rev B* 84(16):165208.
23. Glinka YD, et al. (2013) Ultrafast carrier dynamics in thin-films of the topological insulator Bi_2Se_3. *Appl Phys Lett* 103(15):151903.
24. Panich AM, Shao M, Teske CL, Bensch W (2006) Size-dependent properties of Tl_2Se studied by NMR spectroscopy. *Phys Rev B* 74(23):233305.
25. Taylor R, et al. (2013) A combined NMR and DFT study of Narrow Gap Semiconductors: The case of PbTe. *J Phys Chem C* 117(17):8959–8967.
26. Song Q, et al. (2011) β-detected NMR of Li in $Ga_{1-x}Mn_xAs$. *Phys Rev B* 84(5):054414.
27. Boulouz A, et al. (2001) Transport properties of V-VI semiconducting thermoelectric BiSbTe alloy thin films and their application to micromodule Peltier devices. *J Appl Phys* 89(9):5009–5014.
28. Jeon HW, Ha HP, Hyun DB, Shim JD (1991) Electrical and thermoelectrical properties of undoped Bi_2Te_3-Sb_2Te_3 and Bi_2Te_3-Sb_2Te_3-Sb_2Se_3 single crystals. *J Phys Chem Solids* 52(4):579–585.
29. He L, et al. (2012) Surface-dominated conduction in a 6 nm thick Bi_2Se_3 thin film. *Nano Lett* 12(3):1486–1490.
30. Garnero CF, Gyawali P, Lermechin A, Pegg IL, Philip J (2013) Magnetic properties and Raman spectroscopy of Cr-doped bismuth telluride nanotubes. *J Mater Sci Res* 2(3):68–74.
31. Kou XF, et al. (2012) Magnetically doped semiconducting topological insulators. *J Appl Phys* 112(6):063912.
32. Zhang D, et al. (2012) Interplay between ferromagnetism, surface states, and quantum corrections in a magnetically doped topological insulator. *Phys Rev B* 86(20):205127.
33. Zhou Z, Chien YJ, Uher C (2006) Thin film dilute ferromagnetic semiconductors $Sb_{2-x}Cr_xTe_3$ with a Curie temperature up to 190 K. *Phys Rev B* 74(22):224418.
34. von Bardeleben HJ, et al. (2013) Ferromagnetism in Bi_2Se_3:Mn epitaxial layers. *Phys Rev B* 88(7):075149.
35. Fahnle M, Souletie J (1986) The generalized Curie-Weiss law. *Phys Status Solidi* 138(1):181–188.
36. Arrott AS (1985) Generalized Curie-Weiss law. *Phys Rev B Condens Matter* 31(5):2851–2856.
37. Landau LD, Lifshitz EM (1969) *Statistical Physics* (Pergamon, London), 2nd Ed.
38. Zhang R, Willis RF (2001) Thickness-dependent Curie temperatures of ultrathin magnetic films: Effect of the range of spin-spin interactions. *Phys Rev Lett* 86(12):2665–2668.
39. Voigt J, et al. (1990) Magnetic hyperfine fields in ultrathin Ni films on Cu(100). *Appl Phys, A Mater Sci Process* 51(4):317.
40. Voigt J, et al. (1990) Magnetic hyperfine field at 111In probes in the topmost atomic layer of Ni(111) surfaces. *Phys Rev Lett* 64:2202.
41. Rausch R, Nolting W (2009) The Curie temperature of thin ferromagnetic films. *J Phys Condens Matter* 21(37):376002.
42. Lang M, et al. (2013) Competing weak localization and weak antilocalization in ultrathin topological insulators. *Nano Lett* 13(1):48–53.
43. Ziegler J, Ziegler MD, Biersack JP (2010) SRIM-The stopping and range of ions in matter. *Nucl Instr Meth Phys Res* 268:1818–1823.
44. Misra S, et al. (1987) Theory of the Knight shift in narrow-gap semiconductor. *J Phys C Solid State Phys* 20(2):277–289.
45. Clogston, AM, Jaccarino, V, Yafet Y (1964) Interpretation of Knight shifts and susceptibilities of transition metals: Platinum. *Phys Rev* 134(3A):A650–A661.
46. Schwenzer B, Hu J, Morse DE (2011) Correlated compositions, structures, and photoluminescence properties of gallium nitride nanoparticles. *Adv Mater* 23(20):2278–2283.
47. MacFarlane WA, et al. (2014) $^8Li^+$ β-NMR in the cubic insulator MgO. *J Phys: Conf Ser* 551:012033.
48. Pastawski HM, Gascon JA (1997) NMR line shape in metallic nanoparticles: A matrix continued fractions evaluation. *Phys Rev B* 56(8):4887–4892.
49. Mauri F, Pfrommer BG, Louie SG (1999) Signatures of surface states on NMR chemical shifts: A theoretical prediction. *Phys Rev B* 60(4):2941–2945.
50. van der Klink JJ, Brom HB (2000) NMR in metals, metal particles and metal cluster compounds. *Prog Nucl Magn Reson Spectrosc* 36(2):89–201.
51. Nowak B, Kaczorowski D (2014) NMR as a probe of band inversion in topologically nontrivial half-Heusler compounds. *J Phys Chem C* 118(31):18021–18026.
52. Yu X, et al. (2013) Separation of top and bottom surface conduction in Bi_2Te_3 thin films. *Nanotechnology* 24(1):015705.
53. He L, et al. (2013) Evidence of the two surface states of $(Bi_{0.53}Sb_{0.47})_2Te_3$ films grown by van der Waals epitaxy. *Sci Rep* 3:3406.
54. Lang M, et al. (2012) Revelation of topological surface states in Bi_2Se_3 thin films by in situ Al passivation. *ACS Nano* 6(1):295–302.
55. Tang J, et al. (2014) Electrical detection of spin-polarized surface states conduction in $(Bi_{0.53}Sb_{0.47})_2Te_3$ topological insulator. *Nano Lett* 14(9):5423–5429.